Supplementary Information

Low-temperature ambient-air synthesis of an efficient and stable axial N-coordinated Fe single-atom catalysts for oxygen reduction

Xianghui Wang[a], Yun Luo[a], Xuehan Zheng[b], Zhicheng Wang[a], Shengpin Wu[a], Chenghang You[a]*, Guifa Long[c]*, Jiali Mu[d]*, Zhenxing Liang[e]*

[a]Key Laboratory of Water Pollution Treatment and Resource Reuse of Hainan Province, School of Chemistry and Chemical Engineering, Hainan Normal University, Haikou 571158, China;

[b]School of Chemistry and Chemical Engineering, Hainan University, Haikou 570228, China;

[c]Guangxi Key Laboratory of Chemistry and Engineering of Forest Products, School of Chemistry and Chemical Engineering, Guangxi Minzu University, Nanning 530008, China

[d]China University of Mining and Technology, Xuzhou, 221116, China

[e]Guangdong Provincial Key Laboratory of Fuel Cell Technology, School of Chemistry and Chemical Engineering, South China University of Technology, Guangzhou, 510641, China

*Corresponding authors: you.ch@hainnu.edu.cn; gflong@gxmzu.edu.cn; mjl0726@163.com; zliang@scut.edu.cn

Experimental

Preparation of catalysts

The catalyst PA-PMDA/C were fabricated via a facile one-step strategy (Fig. 1a). The detailed preparation procedure is as follows: 0.65 g of phthalic anhydride (PA), 0.125 g of pyromellitic dianhydride (PMDA), 9.47 g of urea, 0.2 g of ferrous chloride ($FeCl_2$), and 1 g of carbon powder were placed in an agate mortar and thoroughly ground and mixed. The mixed powder was then transferred into a porcelain boat and heated at 180 ℃ for 3 h in a muffle furnace. After naturally cooling to room temperature, the obtained solid was ground into powder and added to 200 mL of 6 M hydrochloric acid solution, followed by magnetic stirring for 4 h and centrifugation to collect the solid product. The solid was washed repeatedly with deionized water and centrifuged until the pH value of the supernatant reached 7. Finally, the obtained solid was dried overnight at 60 ℃ in a vacuum drying oven to obtain the target catalyst (PA-PMDA/C). For comparison, the catalysts without PMDA and carbon, and the one without sole PMDA were prepared, which were entitled as PA and PA/C, respectively. Also, the carbon supported iron phthalocyanine (FePc/C) was obtained by simply mixing FePc and carbon powder.

Preparation of working electrodes

For electrochemical measurements, a glassy carbon electrode (GCE, Φ 5 mm) was used as the working electrode substrate. Before every measurement, the GCE was cleaned by ethanol in an ultrasonic bath, polished with α-Al_2O_3 slurry (50 nm) on a micro cloth, and rinsed with DI water.

For catalysts ink preparation, 5.0 mg catalyst and 1 mL Nafion ethanol solution (0.25 wt%) were thoroughly mixed under ultrasound for about 30 min. And then, 20 μL slurry was coated onto the GCE and dried naturally. The catalyst loading was calculated to be 0.5 mg cm^{-2}. For comparisons, a commercial Pt/C (20 wt%, Johnson Matthey Corp.) catalyst was also used for ORR.

Preparation of air electrode

For air electrode preparation, a Toray carbon paper (TGP-H-060) was used as the substrate. A diffusion layer was formed by painting the suspension of carbon black (XR-72R) and polytetrafluoroethylene (PTFE) onto one side of the carbon paper (the mass ratio of carbon black and PTFE is 3:2).

For catalyst layer fabrication, a catalyst ink was first prepared through the same procedure described in the working electrode preparation. The ink obtained was painted onto the other side of carbon paper and dried under an infrared lamp. The catalyst loading for PA-PMDA/C is calculated to be 1.0 mg cm^{-2}. For comparisons, Pt/C (20 WT%) was also used to fabricate an air electrode through the same procedures.

Characterization

The scanning electron microscopy (SEM) images were obtained on a JSM-7100F field emission scanning electron microscope (JEOL, Japan), with an acceleration voltage of 5 kV. The transmission electron microscopy (TEM) was operated on a JEM-2100 transmission electron microscope (JEOL, Japan) at an acceleration voltage of 200 kV. The X-ray photoelectron spectroscopy (XPS) was conducted on an ESCALAB 250 X-ray photoelectron spectrometer (Thermo-VG Scientific, USA).

The morphologies and nanostructures of the catalysts were characterized using scanning electron microscopy (SEM) and transmission electron microscopy (TEM). SEM analyses were performed on a JSM-7100F field emission SEM (JEOL, Japan) at an accelerating voltage of 5 kV. TEM observations were carried out on a JEM-2100 TEM (JEOL, Japan) operated at 200 kV. The surface atomic compositions of the catalysts and their precursors were determined using X-ray photoelectron spectroscopy (XPS) on an ESCALAB 250 spectrometer (Thermo-VG Scientific, USA) with monochromatized Al Kα radiation. N_2 adsorption-desorption isotherms were measured at 77 K using a Tristar II 3020 automated surface area and porosimetry system (Micromeritics, USA).

Electrochemical Measurements

To assess the electrochemical performance of the catalysts, a three-electrode glass cell system was utilized. Prior to each measurement, the 0.1 M KOH electrolyte was saturated with 99.999% O_2 for at least 30 minutes to ensure a fully oxygenated environment. All electrochemical experiments were conducted at ambient temperature using a CHI760D electrochemical workstation (CHI, China), integrated with a rotating ring-disk electrode (RRDE) setup (Gamry, USA). The electrochemical configuration included an Hg/HgO/KOH (1 M) electrode (Gaoss Union, China) as the reference and a graphite rod as the counter electrode. The initially measured potentials versus Hg/HgO/KOH (1 M) were converted to the reversible hydrogen electrode (RHE) scale using the Nernst equation:

$$E_{vs.\ RHE} = E_{vs.Hg/HgO} + E^{\theta}_{Hg/HgO} + 0.059pH.$$

where the $E^{\theta}_{Hg/HgO}$ value was 0.098 V. All current densities were normalized to the GCE's geometric area (0.1964 cm^2). No IR compensation was applied during the electrochemical performance measurements.

Rotating ring-disk electrode (RRDE) measurements were performed at a rotation speed of 1600 rpm in an O_2-saturated 0.1 M KOH solution. The glassy carbon disk was paired with a Pt ring, maintained at a bias voltage of 1.42 V (vs. RHE). The peroxide yield (η) and electron transfer number (n) per oxygen molecule were calculated using the following equations:

$$\eta = 200I_r(NI_d + I_r)^{-1}$$

$$n = 4I_d(I_d + I_rN^{-1})^{-1}$$

where I_r and $I_d$are the ring and disk currents, respectively, and N is the collection efficiency, confirmed to be 0.36 based on the reduction of $K_3Fe(CN)_6$.

The methanol tolerance and stability of the catalysts were evaluated using chronoamperometry measurements at a potential of 0.72 V (vs. RHE), a potential falling within the typical practical working

potential window for energy devices such as zinc-air batteries and proton exchange membrane fuel cells.

The electrochemical surface area (ECSA) was calculated using the following equation:

$$ECSA=C_{DL}/Cs$$

where C_{DL} is the double-layer capacitance and *Cs* is the specific capacitance, characterized as 0.040 mF/cm² in 1 M KOH electrolyte. This value serves as a reference parameter for the ECSA calculation.

Battery tests

A home-made ZAB device was designed for the tests. A 6 M KOH solution containing 0.2 M zinc acetate was used as the electrolyte, and a zinc foil was used as the anode, respectively. Before assembly, the Zn foil was polished, rinsed with dilute HCl solution (2 M) and deionized water, and dried in vocuum. The discharge-charge polarization curves were obtained by an CHI760E potentiostat (CHI, China). The full-discharge experiment was conducted by using galvanostatic technology on a CT3004K battery testing system (LANHE, China) under the current density of 10 mA cm^{-2}.

Simulations results of XANES simulations

The simulations were performed using the FDMNES program, which is based on the Finite Difference Method (FDM) to solve the Schrödinger equation and uses the Green formalism (multiple scattering) on a muffin-tin potential. During the XANES simulations of Fe sample, the models for simulations were constructed according to the EXAFS curve fittings. The final states were calculated in a Fe-atomcentered sphere with a fixed radius, with the atoms inside the sphere considered in the calculation. To achieve a balance between the good calculation and time spending, a radius of 7 Å was selected for the sphere.

Calculation details

All the density functional theory (DFT) calculations were performed by using Vienna Ab-initio Simulation Package (VASP) code[2, 3] with electron correction treated within the generalized gradient approximation using the Perdew-Burke-Ernzerhof (PBE) exchange-correlation functional[4, 5]. The

projector augmented wave (PAW) method[6] was used to treat the effect of the inner cores on the valence states. The reaction on the surface of catalyst is carried out using the models composed of p(7x7) supercells. In all the calculations, the cutoff energy was set to be 500 eV and Gaussian electron smearing method with σ = 0.05 eV were used. The convergence tolerance for residual force and energy on each atom during structure relaxation was set to 0.05 eV/Å and 10^{-5} eV, respectively. The Monkhorst-Pack grids[7] were set to be 2×2×1 the structure optimizations and energy optimizations. A vacuum layer of 20 Å along the z direction was introduced to eliminate the spurious interactions between adjacent sheets. A dispersion correction method (DFT-D3) were performed to account for van der Waals interactions of adsorbates and different catalysts. Here, we perform ELF calculations based on the optimized converged structural model to obtain the electronic local distribution states.

The adsorption-free energies of above reaction intermediate (*ΔG*) are usually considered as an effective descriptor for ORR activity. The Gibbs free energy of (*ΔG*) can be calculated by the following equation: $\Delta G = \Delta E + \Delta E_{ZPE} - T\Delta S + \Delta G_U + \Delta G_{pH}$. where ΔE, ΔE_{ZPE}, and ΔS are the reaction energy of a given reaction step on the given unit cell, the difference corresponding to the zero-point energy between the adsorbed reaction intermediate and free state and the entropy change of intermediate adsorption, respectively. $\Delta G_U = -eU$, here U is the potential at the electrode and e is the transferred charge. $\Delta G_{pH} = k_B T \times \ln_{10} \times pH$, where k_B is the Boltzmann constant and T =300 K. In this work, the influence of pH was neglected. The free energy of O_2 is obtained from the reaction $O_2 + 2H_2 \rightarrow 2H_2O$, which is 4.92 eV at 300K and pressure of 0.035 bar. The entropies of molecules (including O_2, H_2 and H_2O, etc.) in the gas (or liquid) phase are taken from the "CRC Handbook of Chemistry and Physics".

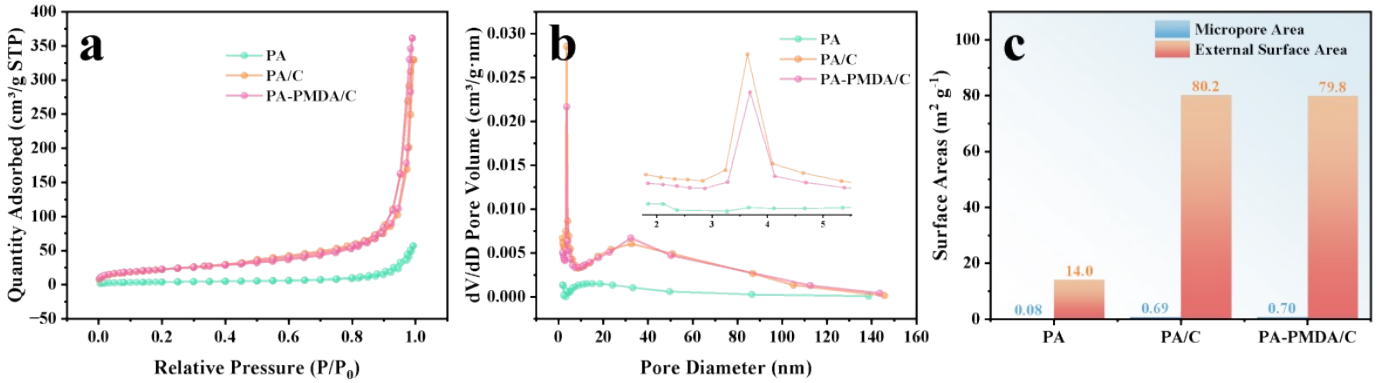

Fig. S1 (a) N_2 adsorption-desorption isotherms for different catalysts; (b) pore-size distributions; (c) BET surface areas

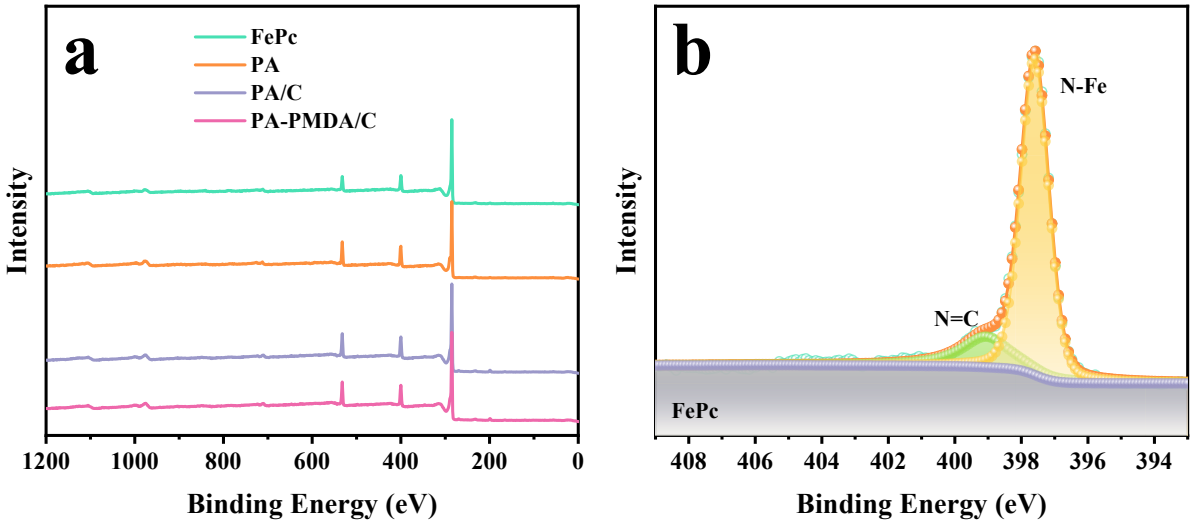

Fig. S2 (a) XPS spectra for various catalysts; (b) N1s spectra for FePc.

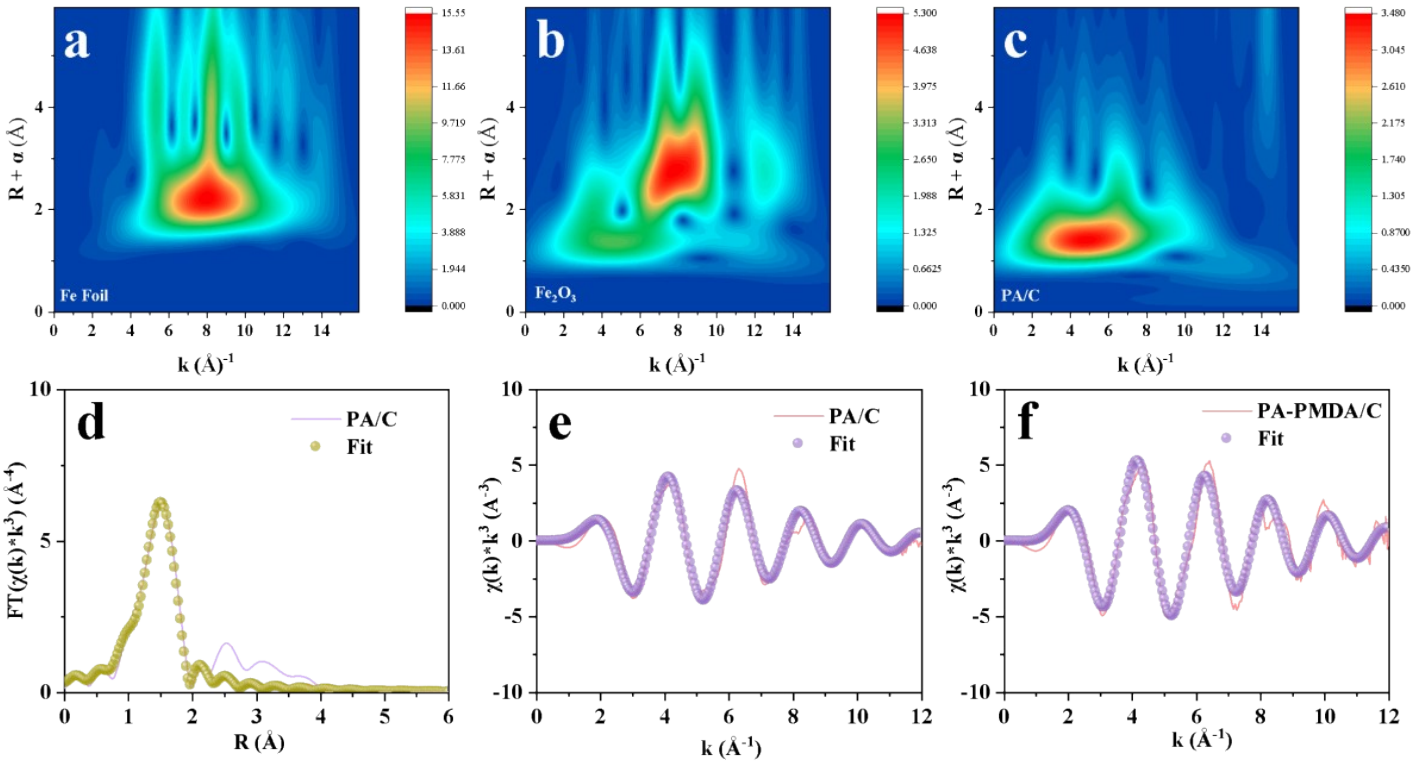

Fig. S3 wavelet transformed EXAFS for (a) Fe foil; (b) Fe_2O_3; (c) PA/C. (d) FT-EXAFS fitting result of PA/C; (e) K space and relative fitting results for PA/C; (f) K space and relative fitting results for PA-PMDA/C

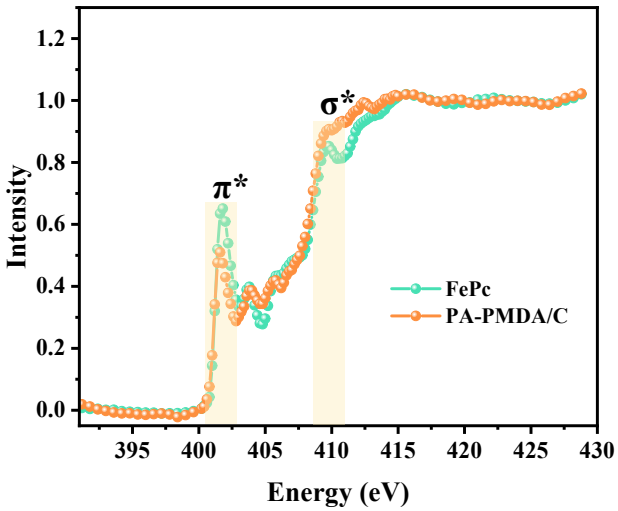

Fig. S4 N K-edge spectra of FePc and PA-PMDA/C

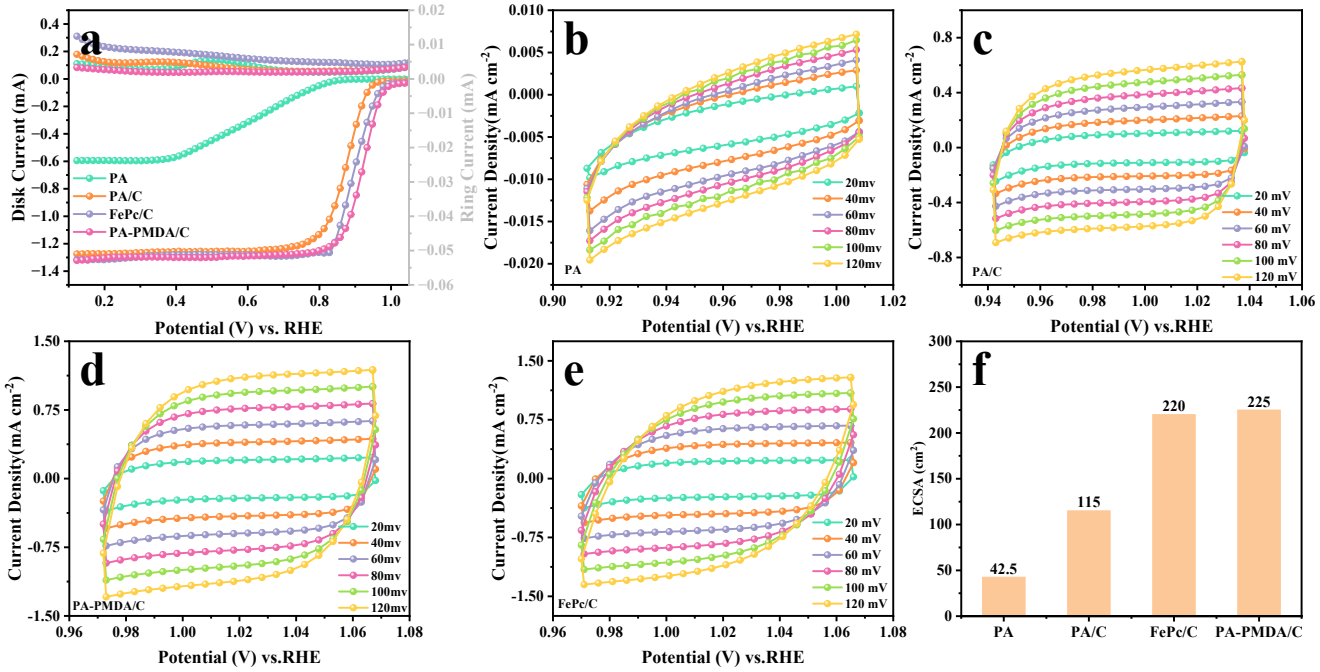

Fig. S5 (a) RRDE measurements results; CV curves under different scanning rates: (b) PA; (c) PA/C; (d) PA-PMDA/C; (e) FePc/C; (f) ECSA

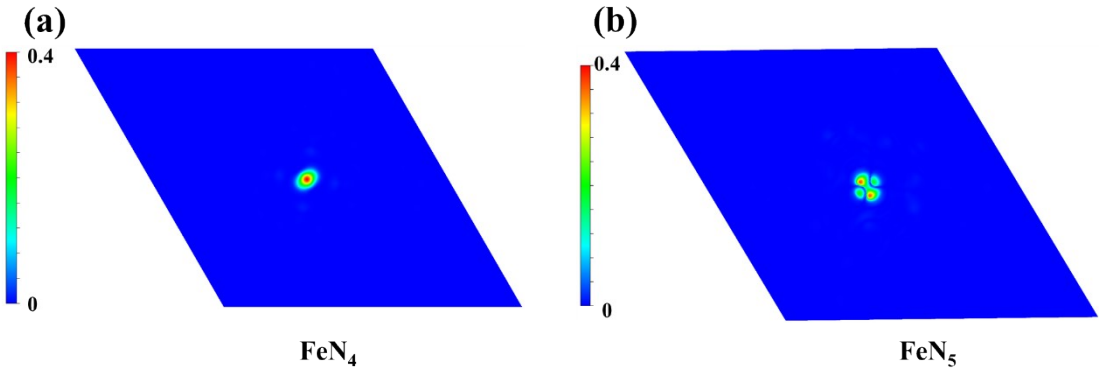

Fig. S6. Planar distribution maps of the spin polarization for (a) FeN_4 and (b) FeN_5, models from the top-view. The red iso-surfaces represent the spin-up states, while the blue iso-surfaces represent the spin-down states.

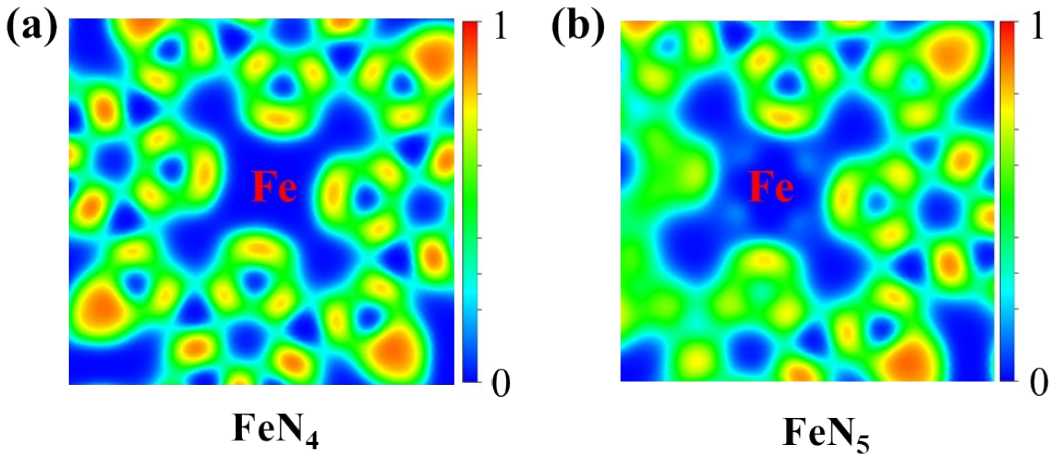

Fig. S7. ELF analyses of Fe atoms in (a) FeN_4 and (b) FeN_5 models from the top-view.

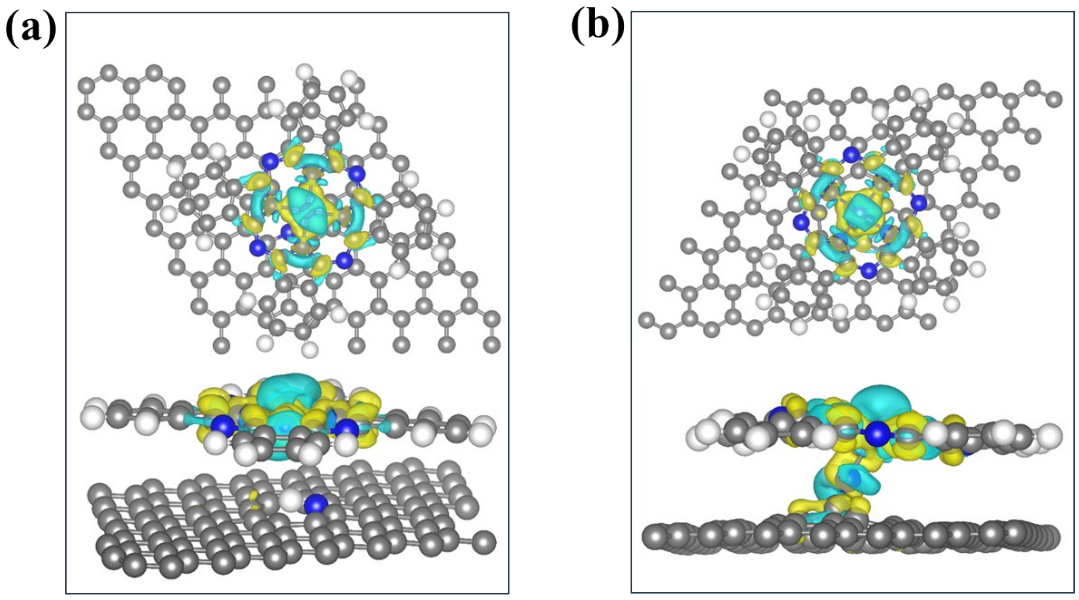

Fig. S8. The 3D difference charge density of FeN_5 and FeN_4 models. The yellow and cyan areas, respectively, represent the increase and decrease in density. The white, gray, blue, and grayish purple balls refer to hydrogen, carbon, nitrogen, and iron atoms, respectively.

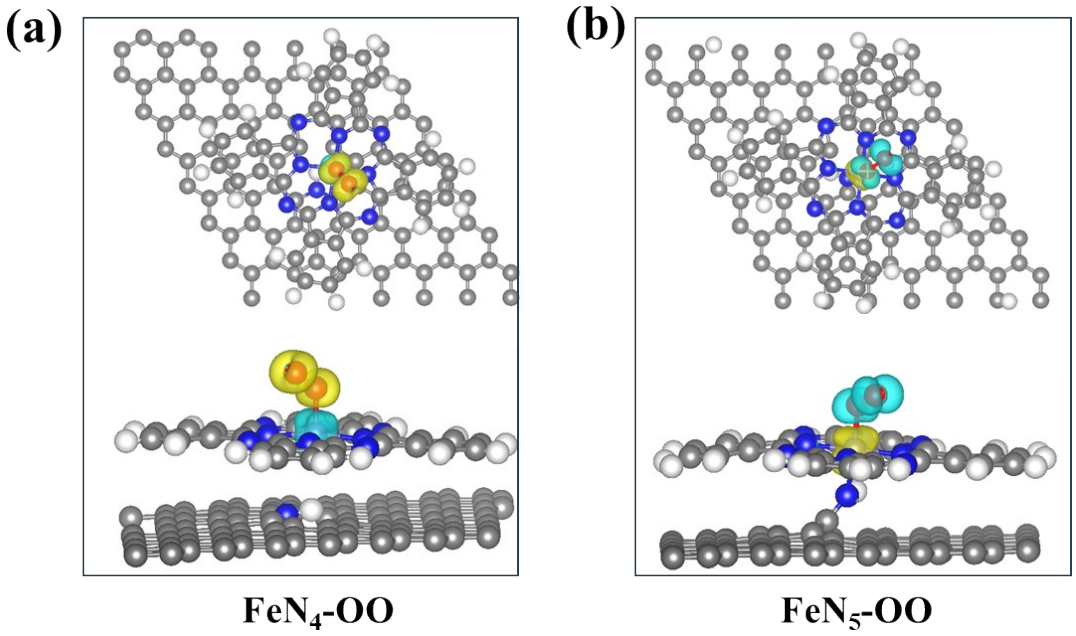

Fig. S9. Spin density distribution of (a) FeN_4 and (b) FeN_5 models interreacted with adsorbed O_2. The yellow and cyan areas, respectively, represent the positive and negative difference of spin-up and spin-down electrons spin state.

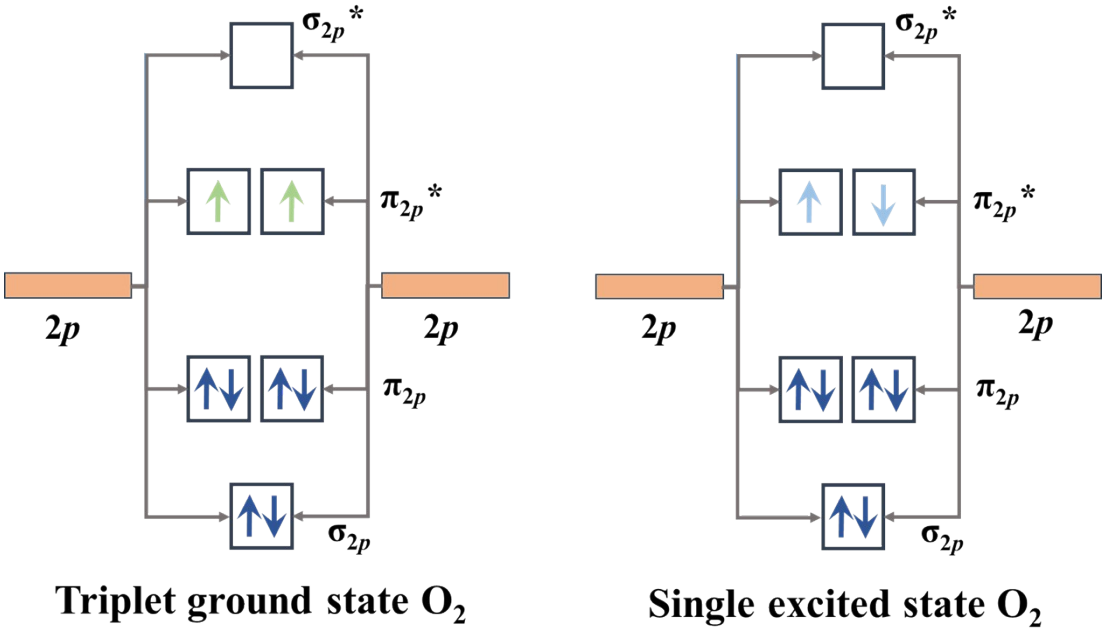

Fig. S10. Comparison the spin flip energy diagram of O_2 molecule with different states.

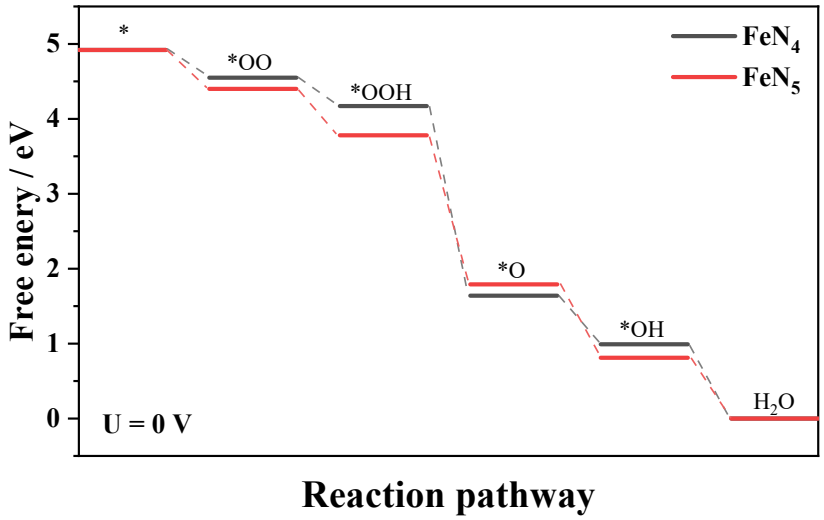

Fig. S11. Gibbs free energy of ORR intermediates adsorbed on FeN_4 and FeN_5 models at pH = 1 under U = 0 V.

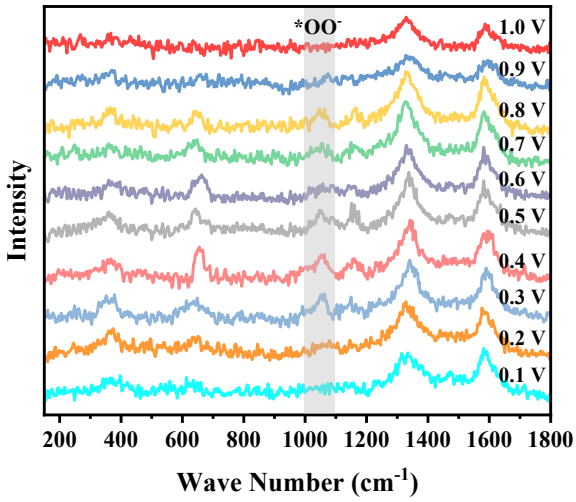

Fig. S12 In-situ Raman spectra for PA-PMDA/C

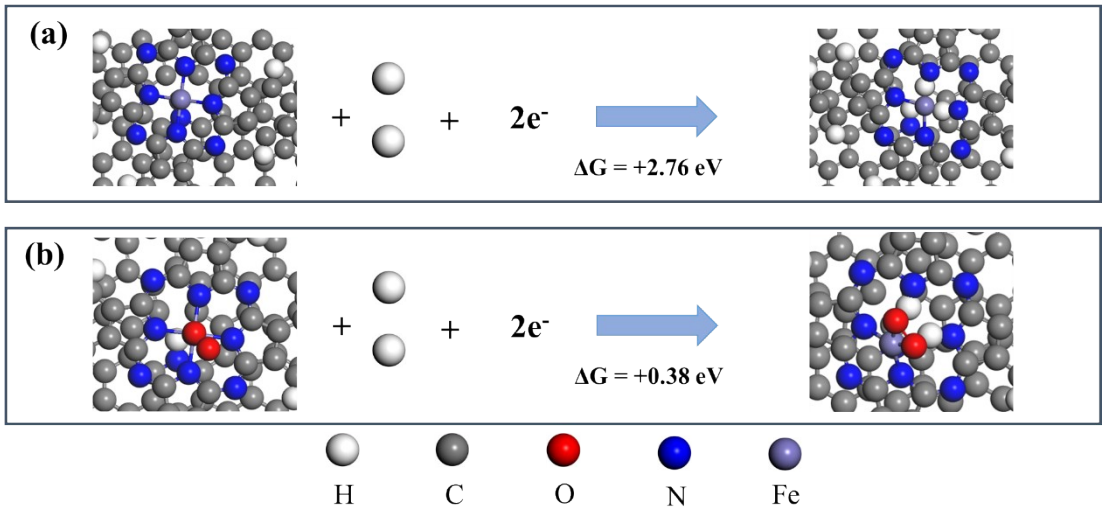

Fig. S13. Atomistic structures of simulation models for leaching of the central M atoms in FeN_4 active sites, (a)FeN_4 and (b) FeN_4-O_2. In the Fig. , the white, grey, blue, red, and grayish purple balls represent H, C, N, O, and Fe atoms, respectively.

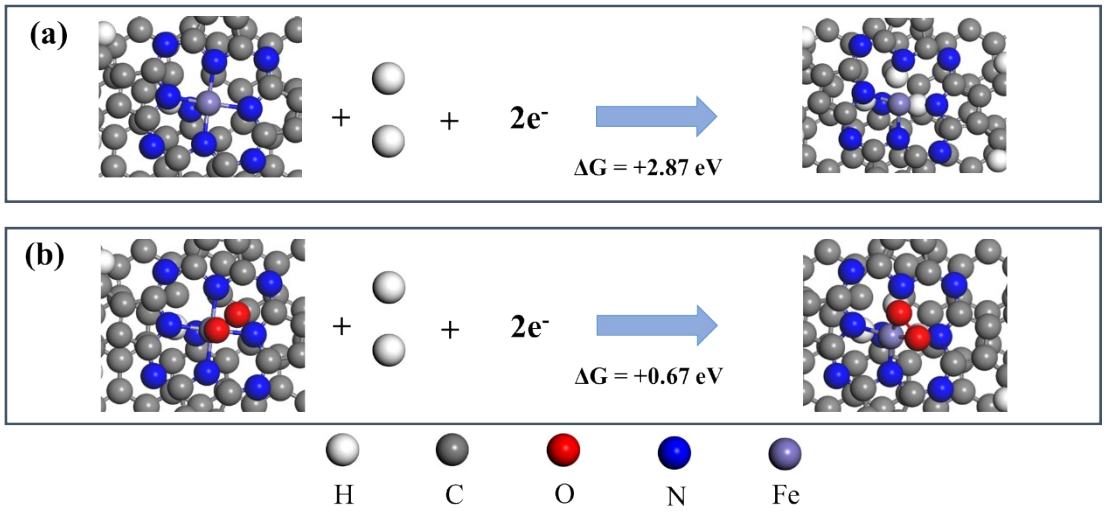

Fig. S14. Atomistic structures of simulation models for leaching of the central M atoms in FeN_5 active sites, (a)FeN_5 and (b) FeN_5-O_2. In the Fig. , the white, grey, blue, red, and grayish purple balls represent H, C, N, O, and Fe atoms, respectively.

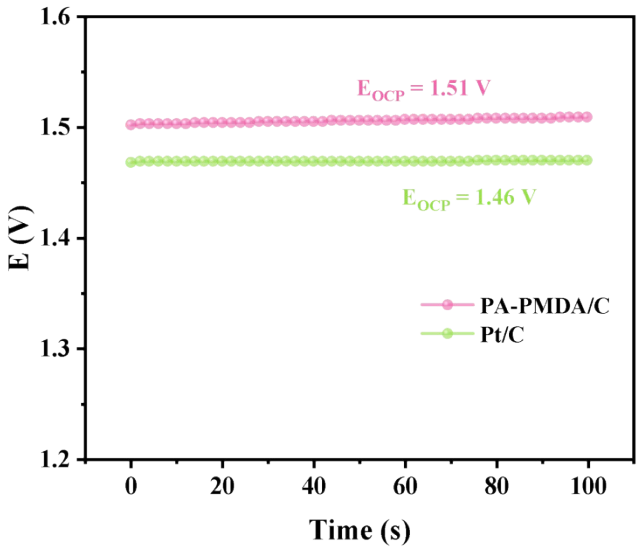

Fig. S15 Open circle potentials of PA-PMDA/C and Pt/C catalysts based ZAB

Table S1 Fe K-edge EXAFS spectra fitting parameters

Sample	Path	CN	R (Å)	σ^2 ($\times10^{-3}$ Å^2)	ΔE_0 (eV)	R (%)
Fe foil	Fe-Fe_1	8*	2.46±0.01	4.9±1.5	6.15±2.34	0.6
	Fe-Fe_2	6*	2.85±0.01	5.5±2.6		
Fe_2O_3	Fe-O	6*	1.98±0.03	13.4±4.4	-3.57±2.84	1.6
FePc/C	Fe-N	4*	1.97±0.01	7.7±1.8	1.89±1.36	0.6
PA	Fe-N	4.3±0.3	1.99±0.01	7.6±1.3	-2.72±0.86	0.3
PA/C	Fe-N	4.6±0.4	1.99±0.01	8.7±1.7	-3.19±1.24	0.2
PA-PMDA/C	Fe-N	5.3±0.3	2.00±0.01	7.5±0.9	-0.67±0.62	0.2

Table S2. Comparison of ORR performance for PA-PMDA/C in alkali solution, as well as other Pt-free group catalysts reported in the literatures.

No.	Catalysts	Electrolyte	E_{onset} (V vs. RHE)	$E_{1/2}$ (V vs. RHE)	References
	PA-PMDA/C	**0.1M**	**0.102**	**0.92**	**Our work**
1	FeSA-Fe_3C/NC	0.1M	1.007	0.902	[1]
2	CeO_2-Co-N-C	0.1M	0.99	0.90	[2]
3	FeNC-V_N	0.1M	0.990	0.902	[3]
4	Co@Tb_2O_3	0.1M	1.02	0.85	[4]
5	Co-N-3-C/CNT	0.1M	1.04	0.887	[5]
6	Mo/C tubes	0.1M	0.86	0.81	[6]
7	Fe–N4SP/NPS-HC	0.1M	1.01	0.912	[7]
8	JUC-650	0.1M	0.90	0.72	[8]
9	Fe@CNT@CuNC	0.1M	0.95	0.86	[9]
10	BDA-COF	0.1M	0.86	0.74	[10]
11	Py-COF-αβ	0.1M	0.89	0.77	[11]
12	MoP@Mn-SAC-NC	0.1M	1.02	0.894	[12]
13	$MF_{0.04}$/CN	0.1M	0.94	0.79	[13]
14	Gd-N-C	0.1M	0.97	0.89	[14]
15	FeNS/C	0.1M	1.015	0.91	[15]
16	Fe–N_4SP/NPS-HC	0.1M	1.016	0.901	[16]
17	CNP-900	0.1M	0.94	0.77	[17]
18	Fe_3O_4/CeO_2@N-	0.1M	0.99	0.84	[18]
19	TaOx/rGO-$CNF_{0.5}$	0.1M	0.82	0.68	[19]
20	FeV-DAS-NC	0.1M	1.03	0.89	[20]

Table S3. Performance comparison between the as-prepared PA-PMDA/C and the reported materials for ZABs.

No.	Catalysts	Electrolyte	Power density ($mW\ cm^{-2}$)	References
	PA-PMDA/C	**6 M KOH/0.2 M $Zn(OAc)_2$**	**209**	**Our work**
1	CeO_2-Co-N-C	6 M KOH/0.2 M $Zn(OAc)_2$	122	[2]
2	BODIPY-Mn-bipy-I	6 M KOH/0.2 M $Zn(OAc)_2$	176	[21]
3	FeSA-Fe_3C/NC	6 M KOH+0.2 M $Zn(Ac)_2$	151.3	[1]
4	Mo_2C-Fe_3N@NCF	6 M KOH+0.2 M $Zn(Ac)_2$	88.4	[22]
5	FeS/Fe_3C@Fe-N-C	6 M KOH	113	[23]
6	Fe-NG	6 M KOH+0.2 M $Zn(Ac)_2$	133	[24]
7	NiFe LDH A-$Fe_{SA}Co_{SA}$-$FeCo_{Alloy}$-CNT/NC	6 M KOH+0.2 M $Zn(Ac)_2$	173	[25]
8	CuMo2ON@NG	6 M KOH+0.2 M $Zn(Ac)_2$	176.3	[26]
9	FeN0.0324@NiN4/C	6 M KOH/0.2 M $Zn(OAc)_2$	180.9	[27]
10	Co-MOF-74-HATP	6 M KOH/0.2 M $Zn(OAc)_2$	96.6	[28]
11	NCMP	6 M KOH/0.2 M $Zn(OAc)_2$	148	[29]
12	Co@C-CoNC	6 M KOH/0.2 M $Zn(OAc)_2$	162.8	[30]
13	CCSO/NC-2	6 M KOH/0.2 M $Zn(OAc)_2$	92	[31]
14	FeSA/AC@HNC	6 M KOH/0.2 M $Zn(OAc)_2$	171.5	[32]
15	NiFeVS	6 M KOH/0.2 M $Zn(OAc)_2$	190	[33]
16	CoSANi-N-CNT/CNF	6 M KOH/0.2 M $Zn(OAc)_2$	132.23	[34]
17	PAM-SC	6 M KOH/0.2 M $Zn(OAc)_2$	107.7	[35]
18	FeCoNiMoW	6 M KOH/0.2 M $Zn(OAc)_2$	116.9	[36]
19	NCNF	6 M KOH/0.2 M $Zn(OAc)_2$	121.1	[37]
20	FePc-BBL COF	6 M KOH/0.2 M $Zn(OAc)_2$	181.4	[38]

References

[1] C.L. Liu, R.Z. Yang, J.C. Wang, B.W. Liu, X.W. Chang, P.X. Feng, X.Z. Zhang, L.J. Zhong, X.L. Zhao, L. Niu, S.Y. Gan, Y.B. Xi, M. Huang, H. Wang, Angewandte Chemie-International Edition 64 (2025).

[2] S. Wang, L. Li, Y. Zheng, C. Xu, Z. Zhuang, K. Sun, W. Yan, J. Zhang, Applied Catalysis B:

Environment and Energy 377 (2025) 125493.

[3] L. Lyu, X. Hu, S. Lee, W. Fan, G. Kim, J. Zhang, Z. Zhou, Y.-M. Kang, Journal of the American Chemical Society 146 (2024) 4803-4813.

[4] X. Wang, J. Zhang, P. Wang, L.C. Li, H.Y. Wang, D.M. Sun, Y.F. Li, Y.W. Tang, X.F. Lu, Y. Wang, G.T. Fu, Energy & Environmental Science 16 (2023) 5500-5512.

[5] C.L. Tang, R. Jin, Y. Xia, Q. Zhang, J.Z. Wang, M.J. Wu, X. Cui, Y.K. Yang, Nano Energy 137 (2025).

[6] Y. Zhao, Z. Zhang, L. Liu, Y. Wang, T. Wu, W. Qin, S. Liu, B. Jia, H. Wu, D. Zhang, X. Qu, G. Qi, E.P. Giannelis, M. Qin, S. Guo, Journal of the American Chemical Society 144 (2022) 20571-20581.

[7] J. Liu, W. Chen, S. Yuan, T. Liu, Q. Wang, Energy & Environmental Science 17 (2024) 249-259.

[8] J.C. Liu, J. Zhao, C.Y. Li, Y.Z. Liu, D.H. Li, H. Li, V. Valtchev, S.L. Qiu, Y.J. Wang, Q.R. Fang, Small 20 (2024).

[9] K. Cheng, Z.Q. Liu, D.M. Jiang, M. Song, Y.Q. Wang, Nano Research 17 (2024) 2352-2359.

[10] G.F. Zhao, X.X. Zou, H. Ma, L.L. Wang, H. Guo, Journal of Energy Chemistry 108 (2025) 83-91.

[11] H.N. Chen, D.H. Li, M. Lin, Q. Wang, Y.H. Zou, J.X. Ran, Y.L. Xing, X.J. Long, Advanced Materials 37 (2025).

[12] Z.Y. Luo, J.Y. Xie, J.S. Cheng, F.L. Wei, S. Lyu, J.J. Zhu, X.F. Shi, X.L. Yang, B. Wu, Z.J. Xu, Advanced Materials (2025).

[13] M. Dan, X.T. Zhang, C.Y. Du, Z. Guo, J.N. Zhang, Z.Q. Liu, Angewandte Chemie-International Edition (2025).

[14] L.D. Dong, C.H. Yu, B.W. Yan, J.W. Li, B. Yang, M.J. Lin, J. Huang, W.L. Xiao, J.B. Zhong, P.K. Shen, Z.Q. Tian, Advanced Functional Materials (2025).

[15] B. Zhang, J.S. Dang, H.Y. Li, J.J. Wang, D.H. Xu, S.H. Jia, M.F. Li, L. Huang, J.G. Duan, Advanced Functional Materials (2025).

[16] Y. Luo, Y. Wang, H. Zhang, Y. Wang, J. Wan, C. Feng, L. Liu, Z. Guo, J. Li, Y. Wang, Energy & Environmental Science 17 (2024) 123-133.

[17] Y.J. Zhao, M.R. Huang, Y.S. Kang, Y. Fang, T.Y. Zhao, H. Wang, J.Y. Ou, J.J. Liu, M.X. Zhong, T. Wang, X.H. Sun, C.Y. Zhao, D. Wang, Energy & Environmental Science 18 (2025) 5298-5308.

[18] J.Y. Liu, J.W. Yin, Y.Z. Lin, M.X. Pang, H. Pang, S.T. Zhang, L. Xu, J. Yang, Y.W. Tang, Nano Research 18 (2025).

[19] D. Sebastián, J.C. Ruiz-Cornejo, M.V. Martínez-Huerta, M.J. Lázaro, Applied Catalysis B: Environment and Energy 374 (2025) 125370.

[20] Q.D. Ruan, R. Feng, L. Liu, L. Zhang, J.J. Feng, Y.C. Shi, Y.J. Gao, A.J. Wang, Chemical Engineering Journal 509 (2025).

[21] W.J. Zhang, Q. Dong, Y.X. Zhao, W.Z. Yang, J.Y. Chen, F.C. Xi, Y.W. Li, X.X. Liu, J. Zhou, Chemical Engineering Journal 507 (2025).

[22] X.-r. Meng, S. Gao, N. Liu, P.-d. Wu, Z. Fang, Chemical Engineering Journal 500 (2024) 157463.

[23] S. Sun, F. Yang, X. Zhang, J. Qian, K. Wei, J. An, Y. Sun, S. Wang, X. Li, Y. Li, Chemical Engineering Journal 487 (2024) 150673.

[24] J. Wang, X. Liu, C.-X. Zhao, Y.-W. Song, J.-N. Liu, X.-Y. Li, C.-X. Bi, X. Wan, J. Shui, H.-J. Peng, B.-Q. Li, J.-Q. Huang, Journal of Energy Chemistry 90 (2024) 511-517.

[25] W.-X. Hong, W.-H. Wang, Y.-H. Chang, H. Pourzolfaghar, I.H. Tseng, Y.-Y. Li, Nano Energy 121 (2024) 109236.

[26] J. Balamurugan, T.T. Nguyen, N.H. Kim, D.H. Kim, J.H. Lee, Nano Energy 85 (2021) 105987.

[27] Q.Q. Liu, J.S. Chen, L.Y. Cao, Y. Wang, Y.R. Qi, Y. Wei, Q.Z. Ma, J.F. Huang, X. Fan, Y.Q. Feng, Advanced Functional Materials (2025).

[28] W. Liu, Y. Liang, M.T. Huo, N. Ma, K.C. Qin, J.F. Chang, Z.H. Xing, Nano Research 18 (2025).

[29] N. Khodayar, A. Noori, M.S. Rahmanifar, M. Moloudi, N. Hassani, M. Neek-Amal, M.F. El-Kady, N.B. Mohamed, X. Xia, Y. Zhang, R.B. Kaner, M.F. Mousavi, Energy & Environmental Science 17 (2024) 5200-5215.

[30] S. Chandrasekaran, R. Hu, L. Yao, L. Sui, Y. Liu, A. Abdelkader, Y. Li, X. Ren, L. Deng, Nano-Micro Letters 15 (2023).

[31] J. Cai, H. Zhang, L. Zhang, Y. Xiong, T. Ouyang, Z.-Q. Liu, Advanced Materials 35 (2023).

[32] H. Zhang, H.-C. Chen, S. Feizpoor, L. Li, X. Zhang, X. Xu, Z. Zhuang, Z. Li, W. Hu, R. Snyders, D. Wang, C. Wang, Advanced Materials 36 (2024).

[33] F.N.I. Sari, Y.-C. Lai, Y.-J. Huang, X.-Y. Wei, H. Pourzolfaghar, Y.-H. Chang, M. Ghufron, Y.-Y. Li, Y.-H. Su, O. Clemens, J.-M. Ting, Advanced Functional Materials 34 (2024).

[34] M.B. Poudel, M.P. Balanay, P.C. Lohani, K. Sekar, D.J. Yoo, Advanced Energy Materials 14 (2024).

[35] M. Jiao, L. Dai, H.-R. Ren, M. Zhang, X. Xiao, B. Wang, J. Yang, B. Liu, G. Zhou, H.-M. Cheng, Angewandte Chemie-International Edition 62 (2023).

[36] R. He, L. Yang, Y. Zhang, D. Jiang, S. Lee, S. Horta, Z. Liang, X. Lu, A.O. Moghaddam, J. Li, M. Ibanez, Y. Xu, Y. Zhou, A. Cabot, Advanced Materials 35 (2023).

[37] N. Li, T.T. Ma, H.H. Wang, J.Y. Li, D.R. Qiu, Z. Meng, J.D. Huang, L.J. Sui, F.M. Han, H.D. Lu, Y.P. Liu, S. Chandrasekaran, Journal of Energy Chemistry 103 (2025) 813-825.

[38] Z. Zhang, W. Wang, X. Wang, L. Zhang, C. Cheng, X. Liu, Chemical Engineering Journal 435 (2022) 133872.